

Brittle failure of orthorhombic borides from first-principles simulationsYidi Shen¹ and Qi An^{1,2,*}¹*Department of Chemical and Materials Engineering, University of Nevada Reno, Reno, Nevada 89577, USA*²*Nevada Institute for Sustainability, University of Nevada, Reno, Nevada 89557, USA*

(Received 6 May 2018; revised manuscript received 16 August 2018; published 11 October 2018)

The orthorhombic boride family XMB_{14} , where X and M are metal atoms, have been of great interest in hard coating applications because of such novel properties as high thermal stability, low density, chemical stability, and a low friction coefficient. However, the brittle failure of orthorhombic borides limits their mechanical stability under working environments and prevents their extended engineering applications. To provide guidelines of improving their stability, we employed density functional theory (DFT) to examine the bonding character and mechanical response of XMB_{14} under pure shear, biaxial shear, and tensile loading conditions. Two typical XMB_{14} compounds, $AlLiB_{14}$ and $Al_{0.75}Mg_{0.78}B_{14}$, were examined to illustrate the effects of intrinsic metal vacancies. We find that the ideal strength for $AlLiB_{14}$ is higher than that for $Al_{0.75}Mg_{0.75}B_{14}$, suggesting that $AlLiB_{14}$ is intrinsically stronger than $Al_{0.75}Mg_{0.75}B_{14}$. The failure mechanism of both $AlLiB_{14}$ and $Al_{0.75}Mg_{0.78}B_{14}$ arises from deconstructing B_{12} icosahedra under pure shear and biaxial shear conditions, while the structural failure under tensile deformation arises from breaking interlayer bonds between icosahedral layers.

DOI: [10.1103/PhysRevB.98.134105](https://doi.org/10.1103/PhysRevB.98.134105)**I. INTRODUCTION**

Hard wear-resistant coatings for machines would be a great benefit in engineering applications because they allow to increase the productivity of expensive automated machines and to save on the current high costs of environmentally hazardous coolants [1]. Orthorhombic borides, formulated as XMB_{14} , where X and M are metal atoms of Al, Mg, Na, Be, and Li, have been of great interest in hard coating applications because they exhibit novel properties such as high thermal stability, low density, chemical stability, and a low friction coefficient [2–5]. Among all orthorhombic borides, $AlMB_{14}$ has some unique characteristics [6–8]. For example, $AlLiB_{14}$ has been found to have less internal distortion and fewer defects than many other XMB_{14} compounds [6,7]. The hardness of $AlMgB_{14}$ can reach to values of 29–41 GPa with a relative low density of 2.59 g/cm [3,8]. In addition, $AlMgB_{14}$ can form thin-film coatings on various substrates, resulting in a surface hardness exceeding 30 GPa [9,10]. Due to these excellent properties, $AlMB_{14}$ has been fabricated using pulsed laser deposition (PLD) and magnetron sputtering techniques [10–12]. Particularly, $AlMgB_{14}$ film with remarkable hardness (> 45 GPa) has been fabricated by PLD technique [10]. In addition, some researchers also focused on depositing $AlMgB_{14}$ films using magnetron sputtering [11,12]. The obtained films have excellent properties in which hardness and Young's modulus are enhanced by 25% and 62% compared to the films fabricated by the PLD technique [11]. However, $AlMB_{14}$ compounds are brittle, which limits their extended engineering applications. To understand their brittle failure behavior, it is essential to understand the deformation and failure mechanisms of $AlMB_{14}$ compounds.

For decades, many theoretical and experimental studies have attempted to measure, state, and understand the mechanical properties of $AlMB_{14}$. The elastic modulus of $AlMB_{14}$ compounds, correlating to the materials strength, have been predicted and measured extensively [7,13,14]. In addition, Raman spectroscopy showed that the extra-icosahedral B-B bonds connecting nearby icosahedra have a greater bond strength than the intra-icosahedral B-B bonds [6]. However, regardless of the high binding strength, recent theoretical study on the cleavage of $AlLiB_{14}$ showed that the easiest cleavage plane among all examined six planes is the {010} plane, which passes B_{12} icosahedral layers along the [001] direction [7]. This is because the {010} plane has a lower number of bond density than other plausible cleavage planes. Therefore, the fracture more likely proceeds between icosahedral layers so that the strength is related to the interlayer B-B bonds that connect the B_{12} icosahedra along [001] direction. Furthermore, the mechanical behavior of $AlMgB_{14}$ has also been investigated under tensile and shear deformation [6,15]. Under tensile deformation, $AlMgB_{14}$ tends to fail along [001] and [010] directions [6]. Under shear deformation, previous density functional theory (DFT) simulations on the $AlMgB_{14}$ suggest that the (001)[100] slip system is the most plausible slip system [15]. For this particular slip system, shear occurs perpendicular to the icosahedral bonds because the boron and metal atoms easily slide toward each other. Despite these efforts, the chemical bonding in $AlMB_{14}$ compounds and their inelastic response to applied stresses are not well established.

The $AlXB_{14}$ compounds ($X = Mg, Na, Li, Y, Tb, Dy, Be, Ho, Er, Yb, \text{ and } Lu$) possess the orthorhombic crystal structure with $Imam$ space group [7,16]. The unit cell contains 64 atoms, including four Al atoms, four X atoms, eight interlayer B atoms (in the form of B_2 pairs), and four B_{12} icosahedra located at (0,0,0), (0,0.5,0.5), (0.5,0,0), and (0.5,0.5,0.5) [2]. Each B atom in the B_2 pair is trigonally bonded to

*Corresponding author: qia@unr.edu

three icosahedra. Two chemically distinct sites were identified in B_{12} icosahedron: six polar sites that directly connect to neighboring B_{12} icosahedra and six equatorial sites that bond to the interlayer B_2 pair [13]. The crystal structures of $AlXB_{14}$ compounds are quite intriguing because of the complex bonding character of B_{12} icosahedron, which requires 26 electrons to stabilize the icosahedral cluster (Wade's rules [17,18]). In particular, for single-crystal $AlMgB_{14}$, its metal lattice sites are not fully occupied, leading to a stoichiometry of $Al_{0.75}Mg_{0.78}B_{14}$ with nearly 25% ordered vacancy concentration [4,19]. However, the processing parameters will affect the degree of ordering of vacancies and may induce microstructural defects [19]. In addition, previous theoretical study showed that the metal atoms in $AlXB_{14}$ are ionized and covalently bonded to B networks by donating their valence electrons [20].

In this article, we applied DFT simulations at the Perdew-Burke-Ernzerhof (PBE) functional level to investigate the chemical bonding and mechanical behavior of $AlMB_{14}$ under pure shear, biaxial shear, and tensile deformation. We selected two typical $AlMB_{14}$ compounds: $AlLiB_{14}$ and $Al_{0.75}Mg_{0.75}B_{14}$. The $AlLiB_{14}$ is selected because it does not contain metal vacancies compared to $Al_{0.75}Mg_{0.75}B_{14}$ (approximately 25% of metal vacancy sites) [3,21]. First, the atomic structure of $Al_{0.75}Mg_{0.75}B_{14}$ is determined from DFT and compared to the known $AlLiB_{14}$. Then, both pure shear and biaxial shear deformation are applied on $AlLiB_{14}$ and $Al_{0.75}Mg_{0.75}B_{14}$ to obtain the critical shear stress and failure mechanism under these loading conditions. Finally, the critical tensile stress and failure mechanism of $AlLiB_{14}$ and $Al_{0.75}Mg_{0.75}B_{14}$ are derived from tensile deformation along the [001] direction.

II. COMPUTATIONAL METHODOLOGY

In this study, we performed all the simulations by applying the DFT method implemented in the VASP package with a plane-wave basis set [22,23]. The PBE functional generalized gradient approximation (GGA) was used for electronic exchange and correlation interaction [24,25]. The projector augmented-wave (PAW) method is used for the core-valence interaction [26]. For the PAW potentials, the $3s^2 3p^1$, $3s^2$, $1s^2 2s^1$, and $2s^2 2p^1$ electrons were treated as valence states for Al, Mg, Li, and B, respectively. The electron partial occupancies were determined using the tetrahedron method with Bloch corrections [27]. The energy cutoff of 600 eV was set in all simulations for the good convergence of energy, force, stress, and geometries. We used the energy convergence of 10^{-5} eV for terminating the electronic self-consistent field (SCF) and the force criterion 10^{-2} eV/Å for geometry optimization. The Kohn-Sham energies are sampled across the Brillouin zone using a Monkhorst-Pack grid scheme with a fine resolution less than $2\pi \times 1/40 \text{ \AA}^{-1}$ for all simulations.

In order to obtain the failure mechanism of $AlLiB_{14}$ and $Al_{0.75}Mg_{0.75}B_{14}$, we examined the deformation behaviors of $AlLiB_{14}$ and $Al_{0.75}Mg_{0.75}B_{14}$ as a function of the tensile strain, pure shear strain, and complex biaxial shear strain that mimics a Vickers indentation experiment. The tensile deformation was performed along a low-index [001] crystal-

lographic direction. For pure shear deformation, we applied shear strain along a particular slip system while relaxing the structure to minimize the other five stress components [28]. In order to mimic the stress under indentation experiment, we implemented the biaxial shear deformation with a biaxial stress distribution beneath an indenter with a shear stress (σ_{xz}) and a normal compressive stress component (σ_{zz}) [29]. The two stress components follow the equation of $\sigma_{zz} = \sigma_{xz} \tan \delta$, where $\delta = 68^\circ$ is the centerline-to-face angle of a Vickers indenter [29]. The residual stresses after relaxing were less than 0.5 GPa for both pure shear and biaxial shear deformation. In the shear deformation, we considered (001)[100], (001)[010], and (001)[110] as plausible slip systems, since they are possible active slip systems based on previous experimental and theory studies [7,19,21]. For shear along the (001)[110] slip system we used a supercell model which contains 128 atoms, while we used the unit cell of 64 atoms for other slip systems and tensile deformation.

The bond breaking is determined by the combination of electron localization function (ELF) analysis [30] and discontinuity of bond length change. The ELF shows the accumulation of localized electron pairs. In addition, the bond stretching ratio as a function of shear strain is applied to investigate the bond breaking.

III. RESULTS AND DISCUSSION

A. Structure and bonding analysis

The atomic structure of $AlLiB_{14}$ is shown in Fig. 1(a) in which a unit cell contains four B_{12} icosahedra, 4 B_2 pairs, four Al, and four Li atoms. In each icosahedron, six B atoms are covalently bonded to six nearby icosahedra and the other six B atoms are bonded to six nearby B_2 pairs. All the atomic structures were visualized using VESTA [31]. Considering crystallographic symmetry, each unit cell contains five different B atoms. The five different sites of B atoms include B1 and B4, which are bonded to icosahedra, B2 and B3 which are bonded to B_2 pairs, and B5 which is bonded to each other to form B_2 pairs, as shown in Fig. 1(c). The distances of inter-icosahedral B-B bond and interlayer B-B bond are 1.74 Å and 1.78 Å, respectively, suggesting that they are covalent bonds. According to Wade's rules [17,18], clusters with $(n + 1)$ pairs of skeleton bonding electrons are called "closo structures." Thus, for $AlLiB_{14}$, each B_{12} icosahedron requires $2 \times (12 + 1) = 26$ electrons to stabilize the closo icosahedral structure. However, 12 B atoms in each icosahedron can only provide 24 electrons, considering that all the B atoms are covalently bonded to nearby icosahedra and B_2 pairs. Thus, four Al atoms and four Li atoms are required to transfer eight electrons to four B_{12} icosahedra to satisfy Wade's rules [17,18]. In B_2 pairs, each B atom is also bonded to three nearby icosahedra. However, the distance of an intrapair B-B bond along [001] direction is 2.08 Å, suggesting they are weakly bonded. Thus, each B in a B_2 pair forms four bonds, which requires two additional electrons for each B_2 pair. Each Al atom is close to two B_2 pairs with the B...Al distance of 2.08 Å. Thus each Al atom can donate two electrons to nearby B_2 pairs. Previous study suggests that the bonding character in $AlLiB_{14}$ can be described as the covalent bond due to the combination of p states

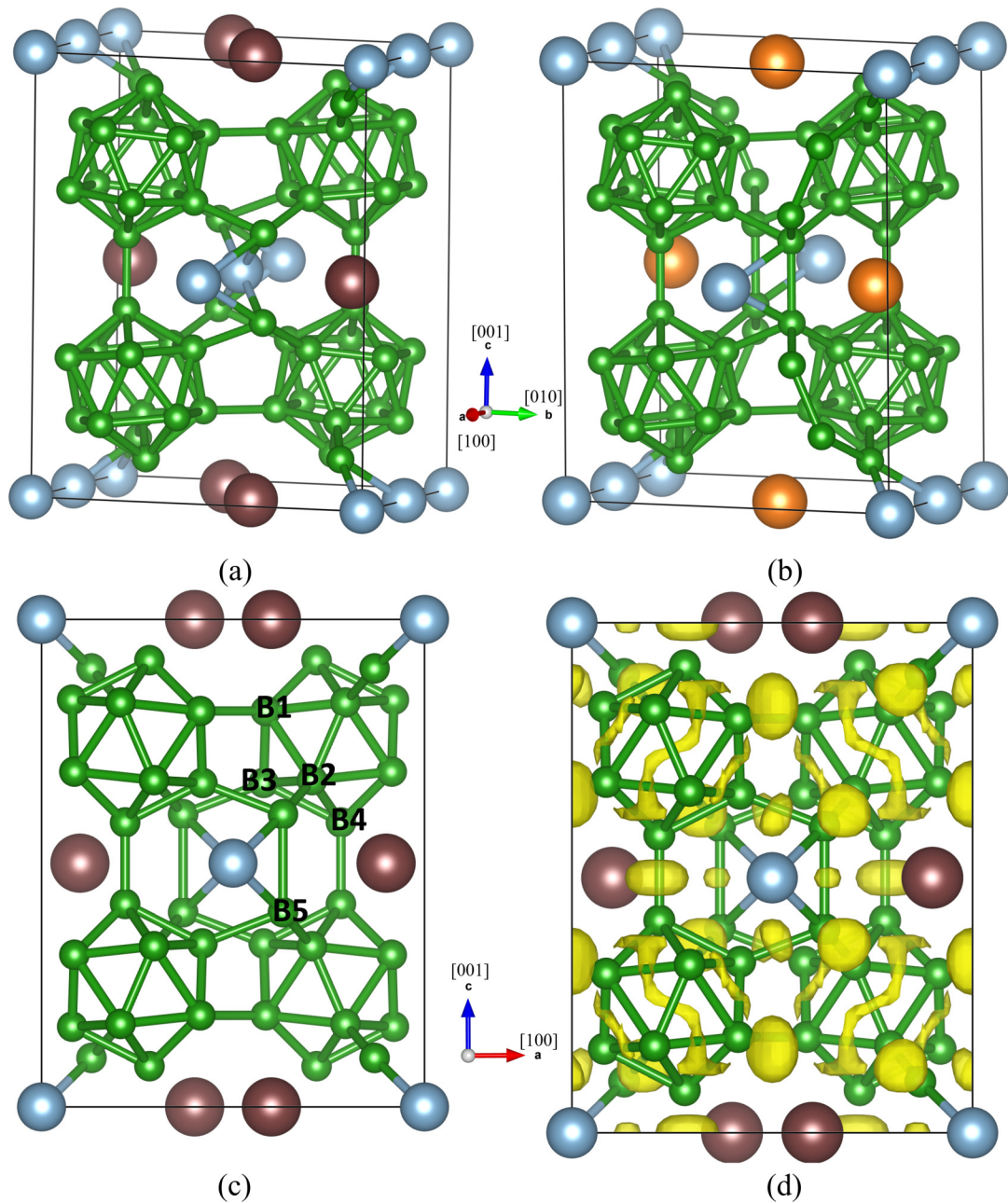


FIG. 1. The crystalline structures of AlLiB_{14} and $\text{Al}_{0.75}\text{Mg}_{0.75}\text{B}_{14}$ and the isosurface of the electron localization function (ELF) for AlLiB_{14} : (a) the AlLiB_{14} structure; (b) the structure of $\text{Al}_{0.75}\text{Mg}_{0.75}\text{B}_{14}$; (c) the AlLiB_{14} structure with different B sites; (d) the isosurface of ELF (0.8) for AlLiB_{14} . The green, blue, brown, and orange balls represent B, Al, Li, and Mg atoms.

from B atoms in B_{12} icosahedron and interstitial B atoms in B_2 pairs [15]. However, our analysis suggests that the structure is stabilized by the donated electrons from the metal atoms [20]. Each Al atom can be regarded as Al^{3+} after it transfers three electrons to B_{12} icosahedra and B_2 pairs [15]. Meanwhile, each Li atom can be regarded as a Li^+ after it contributes one electron to B_{12} icosahedra [15]. This leads to a representation as $\text{Al}^{3+}\text{Li}^+ - (\text{B}_{12})^{2-}(\text{B}_2)^{2-}$ for the AlLiB_{14} structure. To confirm our chemical bonding analysis, we computed the ELF shown in Fig. 1(d). The ELF at 0.8 isosurface level shows the accumulation of localized electron pairs between both icosahedral-pair and inter-icosahedral B atoms, indicating the covalent bonding character of these B-B bonds. The ELF

isosurface between the B_2 pair atoms indicates the covalent bonding character within B_2 pairs, validating the above chemical bonding analysis. In addition, the ELF isosurface near Al and Li atoms on the top and bottom edges also belongs to the B-B bonds which connect two icosahedra along [001] direction, as shown in Fig. S1 of the Supplemental Material (SM) [32].

Replacing Li with a Mg atom will increase the total number of electrons of the system. To satisfy the electron balance in $\text{Al}_4\text{Mg}_4\text{B}_{56}$, one Al and one Mg atom are removed, leading to 25% Mg and Al vacancy concentration. Considering crystallographic symmetry, different distributions of Al and Mg vacancies leads to two different structures: (1) Al

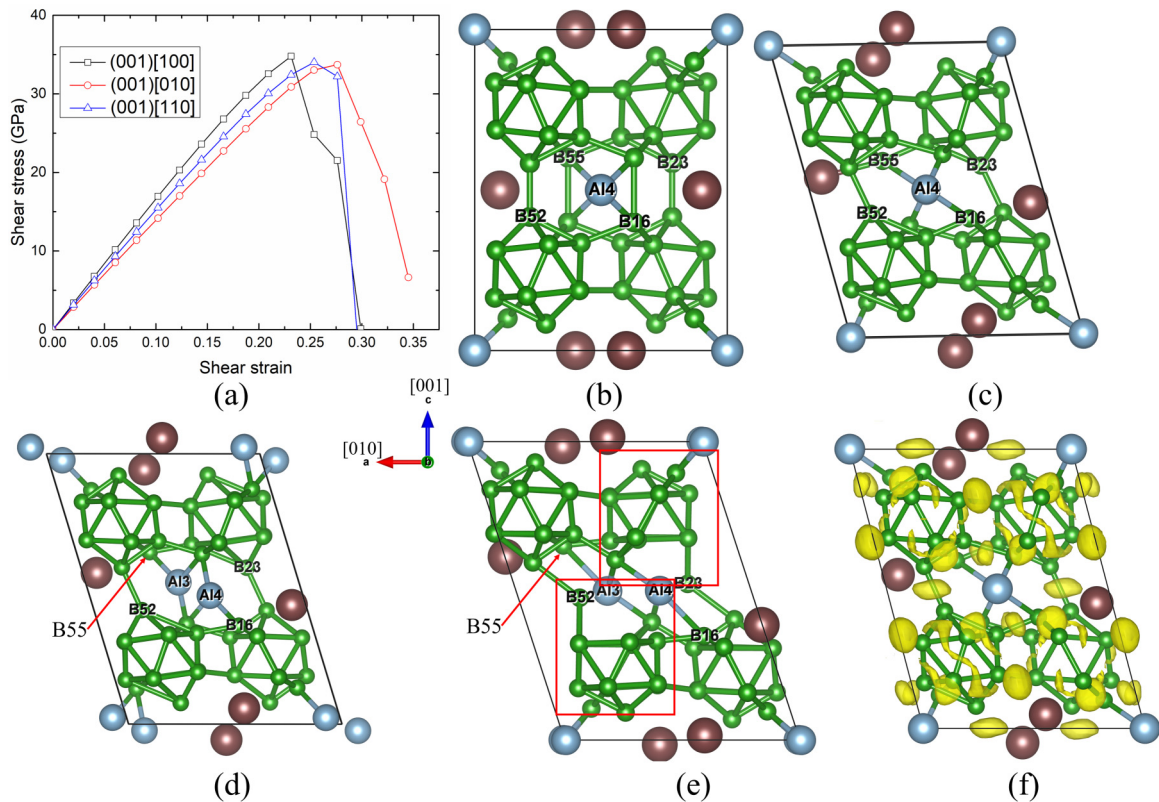


FIG. 2. The shear-stress–shear-strain relationship of AlLiB_{14} under pure shear deformation and the structural evolution for shear along $(001)[010]$ slip system: (a) the shear-stress–shear-strain relationship along three plausible slip systems; (b) the intact structure at zero shear strain; (c) the structure at 0.276 shear strain in which the shear stress reaches its maximum and the interlayer B-B bonds in B_2 pairs break; (d) the structure at 0.299 shear strain before failure in which the Al3-B16 and Al4-B55 bonds break; (e) the failed structure at 0.345 shear strain in which the half of the icosahedra are deconstructed; (f) the ELF of AlLiB_{14} at 0.276 shear strain.

and Mg vacancies are in the same layer along the $[001]$ direction (Fig. S2 of SM); (2) Al and Mg vacancies are in the different layer along the $[001]$ direction [Fig. 1(b)]. Our simulation results show that the second structure is more stable than the first structure by 0.65 eV. Therefore, one Al and one Mg atom are removed from $(0.5, 0.5, 0.5)$ and $(0.25, 0.399, 0)$ sites, respectively. However, considering the bonding character in theoretical $\text{Al}_{0.75}\text{Mg}_{0.75}\text{B}_{14}$ structures, removing one Al and one Mg atoms leads to only one electron deficiency. In addition, the experimental identified structure is $\text{Al}_{0.75}\text{Mg}_{0.78}\text{B}_{14}$, in which the Mg atoms can provide more electrons ($0.03 \times 4 \times 2 = 0.24 e$) per unit cell, which is also not enough for one required electron. This electron deficiency may be caused by the complex defects and microstructures in experimental samples.

B. Deformation and failure of AlLiB_{14} under pure shear deformation

Shear plays an important role in the mechanical failure of boron-related superhard materials [33,34]. To understand the degradation and failure mechanism of AlMB_{14} as hard coating materials, it is essential to examine the failure processes under shear deformation. Therefore, we first examined the shear-induced failure mechanism by applying pure shear deformation on both AlLiB_{14} and $\text{Al}_{0.75}\text{Mg}_{0.75}\text{B}_{14}$. Previous theoretical studies suggested that the (001) plane has the low-

est critical shear stress for both AlLiB_{14} and $\text{Al}_{0.75}\text{Mg}_{0.75}\text{B}_{14}$ [7,19]. We selected $(001)[100]$, $(001)[010]$, and $(001)[110]$ as plausible slip systems under pure shear deformation, since they are possible active slip systems based on experimental and theory studies [3,21,35].

The shear-stress–shear-strain relationship for AlLiB_{14} is displayed in Fig. 2(a). The $(001)[010]$ slip system has the lowest critical shear stress of 33.7 GPa among all three selected slip systems. The critical shear stress for $(001)[100]$ and $(001)[110]$ slip systems are 34.8 GPa and 34.0 GPa, respectively. The critical shear stress under pure shear deformation is defined as the ideal shear strength which is the maximum value that leads to unstable elastic strain. Thus, the $(001)[010]$ slip system is the most plausible activated slip system for AlLiB_{14} . Figures 2(b)–2(f) display the detailed failure mechanism of AlLiB_{14} for shearing along the $(001)[010]$ slip system. Figure 2(b) shows the intact structure at zero shear strain. As the shear strain increases to 0.276, the shear stress increases to its maximum of 33.7 GPa, and the B-B bond in the B_2 pair is stretched from 2.07 Å to 2.48 Å and breaks [Fig. 2(c)]. The B-B bond breaking in B_2 pairs is confirmed by the ELF analysis, as shown in Fig. 2(f). The isosurface between the B_2 pair disappears, suggesting the breakage of the B-B bond. As the system is continuously sheared to 0.299 shear strain, the Al3 and Al4 atoms are stretched away from B16 and B55 atoms, respectively, leading to an increase of Al3...B16 and Al4...B55 distance from 2.09 Å to 3.05 Å and break, as shown

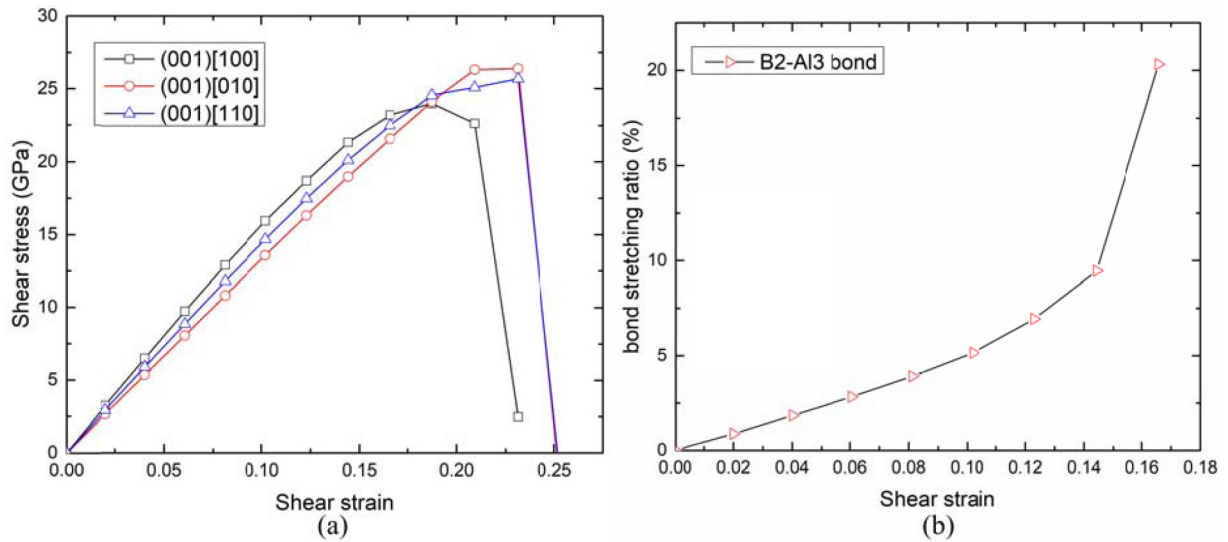


FIG. 3. The shear-stress–shear-strain relationship of $\text{Al}_{0.75}\text{Mg}_{0.75}\text{B}_{14}$ under pure shear deformation and the B2-Al3 bond stretching ratio with the increasing shear strain: (a) the shear-stress–shear-strain relationship and (b) the B2-Al3 bond stretching ratio.

in Fig. 2(d). To further investigate the bond-response process, we also extracted the bond length change of Al4-B55 and Al3-B16 bonds at various shear strain, as shown in Fig. S3(a) of the SM. The stretching ratio of Al4-B55 and Al3-B16 bonds drastically increases from 13.51% to 150.10%, suggesting the breakage of these two bonds. Then as shear strain further increases to 0.345, half of the icosahedra are disintegrated because the icosahedral B23 and B52 atoms are stretched out of icosahedron and the shear stress decreases significantly to 6.63 GPa, as shown in Fig. 2(e). Figure S3(a) of the SM displays a bond stretching ratio of the inter-icosahedral B52-B20 bond that increases significantly from 27.05% to 68.68% at 0.345 shear strain, suggesting breakage of the B52-B20 bond. In order to investigate the effect of vacancy on the mechanical properties of AlLiB_{14} , we also examine the shear stress of $\text{Al}_{0.75}\text{Li}_{0.75}\text{B}_{14}$ with Al and Li vacancy at (0.5,0.5,0.5) and (0.25,0.399,1) sites, respectively. The shear-stress–shear-strain relationship is shown in Fig. S4(a) of the SM. The critical shear stress of $\text{Al}_{0.75}\text{Li}_{0.75}\text{B}_{14}$ with vacancy along (001)[100], (001)[010], and (001)[110] slip systems are 17.9 GPa, 20.2 GPa, and 22.6 GPa, respectively. Thus, the (001)[100] slip system is the most plausible slip system for $\text{Al}_{0.75}\text{Li}_{0.75}\text{B}_{14}$. The ideal shear strength of 17.9 GPa is much lower than AlLiB_{14} (33.7 GPa), suggesting that the metal vacancy sites significantly decrease the ideal shear strength of AlLiB_{14} .

C. Deformation and failure of $\text{Al}_{0.75}\text{Mg}_{0.75}\text{B}_{14}$ under pure shear deformation

The shear-stress–shear-strain relationship for $\text{Al}_{0.75}\text{Mg}_{0.75}\text{B}_{14}$ is shown in Fig. 3(a). The critical shear stress along (001)[100], (001)[010], and (001)[110] slip systems are 24.0, 26.3, and 25.1 GPa, respectively. Thus, the critical stress for (001)[100] is the lowest among these three slip systems, suggesting that it is the most plausible activated slip system for $\text{Al}_{0.75}\text{Mg}_{0.75}\text{B}_{14}$. This most plausible slip system is consistent with the previous DFT study [3]. The failure

mechanism of $\text{Al}_{0.75}\text{Mg}_{0.75}\text{B}_{14}$ shearing along (001)[100] slip system is similar to that of AlLiB_{14} , as shown in Figs. 4(a)–4(f). The failure process is displayed along the $(\bar{1}00)$ plane, not the $(0\bar{1}0)$ plane, because the structural changes can be clearly displayed along the $(\bar{1}00)$ plane. The intact structure is shown in Fig. 4(a). As shear strain increases to 0.166, the B2-Al3 bond is stretched from 2.06 to 2.48 Å and breaks, as shown in Fig. 4(b). This slightly decreases the slope of the shear-stress–shear-strain relationship in Fig. 3(a). To further verify the breakage of this bond, we also extracted the bond length changes during the deformation. Figure 3(b) shows that the B2-Al3 bond stretching ratio drastically increases from 9.46% to 20.32% at 0.166 shear strain, suggesting that the B2-Al3 bond breaks. Figure 4(c) shows the structure at 0.187 shear strain, which corresponds to the maximum shear stress of 24.0 GPa. The interlayer B-B bond in the B_2 pair is slightly stretched from 1.91 to 2.38 Å. However, it is not broken yet. As the shear strain continuously increases to 0.209, the interlayer B-B bond is stretched to 2.84 Å and breaks as shown in Fig. 4(d). Figure S5(a) of the SM shows that the interlayer B-B bond stretching ratio increases from 24.56% to 48.70%, suggesting that this bond breaks. ELF analysis was applied to show the electron pairs between two interlayer B atoms, as shown in Fig. S5(c). The isosurface disappears at 0.209 shear strain, indicating the bond breaking. The combination of breaking the intrapair B-B and B2-Al3 bonds slightly releases shear stress to 22.6 GPa. As shear strain increases to 0.231, half of the icosahedra are disintegrated because the B23 and B52 atoms are stretched out of the icosahedra, as shown in Figs. 4(e) and 4(f). The structure failure causes the shear stress to decrease significantly, from 22.6 to 2.5 GPa. The bond-response process of the inter-icosahedral B52-B32 bond is shown in Fig. S5(a); the breaking of this bond is confirmed by a significant increase of the bond stretching ratio from 12.23% to 99.87%.

The shear-stress–shear-strain relationship of AlMgB_{14} is shown in Fig. S4(b) of the SM. The critical shear stresses for AlMgB_{14} shearing along the (001)[100], (001)[010], and

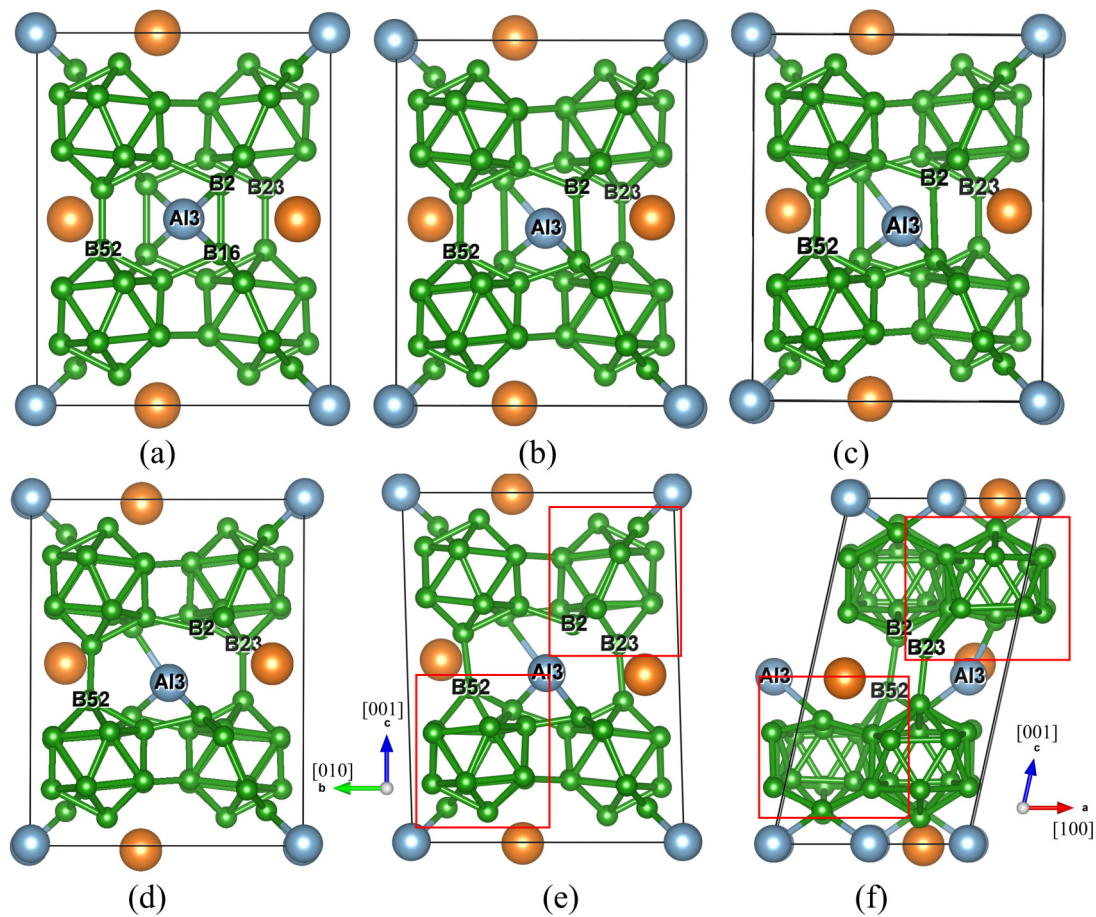


FIG. 4. The structural changes for $\text{Al}_{0.75}\text{Mg}_{0.75}\text{B}_{14}$ shearing along $(001)[100]$ slip system: (a) the intact structure; (b) the structure at 0.166 shear strain in which the inter-icosahedra B2-Al3 bond is stretched from 2.06 Å to 2.48 Å and breaks; (c) the structure at 0.187 shear strain in which the interlayer B-B bond in B_2 pairs is stretched from 1.91 to 2.38 Å without breaking the B_2 pair; (d) at 0.209 shear strain the interlayer B-B bond is stretched to 2.84 Å and breaks; (e) the failed structure at 0.231 shear strain with the deconstruction of the icosahedra; and (f) the failed structure at 0.231 shear strain which is shown along $(0\bar{1}0)$ plane. All structures are viewed along the $(\bar{1}00)$ plane.

$(001)[110]$ slip systems are 24.6, 21.8, and 21.7 GPa, respectively. Thus, the ideal shear strength of AlMgB_{14} is 21.7 GPa, which is lower than that of AlLiB_{14} (33.7 GPa) and $\text{Al}_{0.75}\text{Li}_{0.75}\text{B}_{14}$ (24.0 GPa). This indicates that AlMgB_{14} is intrinsically weaker than AlLiB_{14} , but the presence of metal vacancies slightly increases its critical shear stress because the vacancies balance the electrons in $\text{Al}_{0.75}\text{Li}_{0.75}\text{B}_{14}$, leading to a more stable structure.

In summary, under pure shear deformation, for both AlLiB_{14} and $\text{Al}_{0.75}\text{Mg}_{0.75}\text{B}_{14}$, the icosahedra are disintegrated because the inter-icosahedral B atoms (bonded to nearby icosahedron) are stretched out of icosahedron, suggesting that the B-B bonds which directly connect icosahedra are stronger than the intra-icosahedral B-B bonds. This is consistent with the previous Raman spectroscopy and DFT study results [6,7].

D. Deformation and failure of AlLiB_{14} under biaxial shear deformation

An indentation experiment provides a practical way to examine the mechanical response of materials under deformation. However, the stress condition under the indentation experiment is more complex than the pure shear deformation.

To predict the failure process of AlLiB_{14} and $\text{Al}_{0.75}\text{Mg}_{0.75}\text{B}_{14}$ under indentation experiments, we applied biaxial shear deformation along the $(001)[100]$, $(001)[010]$, and $(001)[110]$ slip systems [29].

The shear-stress–shear-strain relationship for AlLiB_{14} under biaxial shear deformation is displayed in Fig. 5(a). The critical shear stress for $(001)[100]$, $(001)[010]$, and $(001)[110]$ slip systems is 35.6 GPa, 35.5 GPa, and 33.9 GPa, respectively. Therefore, the $(001)[110]$ slip system has the lowest critical shear stress, suggesting that it is the most plausible slip system for AlLiB_{14} under indentation experiments. The most plausible slip system is different from the pure shear deformation, suggesting that the activated slip system is changed under different loading conditions. To understand the atomic failure mechanism of AlLiB_{14} shearing along the $(001)[110]$ slip system, the structures at various critical strains are shown in Figs. 5(b)–5(d). Figure 5(b) displays the intact structure at zero shear strain. At 0.231 shear strain, the shear stress reaches the maximum value of 33.9 GPa and the whole structure is deformed without fracturing the icosahedra and B_2 pairs, as shown in Fig. 5(c). As the system is continuously sheared to 0.254 shear strain, the interlayer B110 and B112 atoms in B_2 pair are stretched away from the Al6 atom [Fig. 5(d)], leading

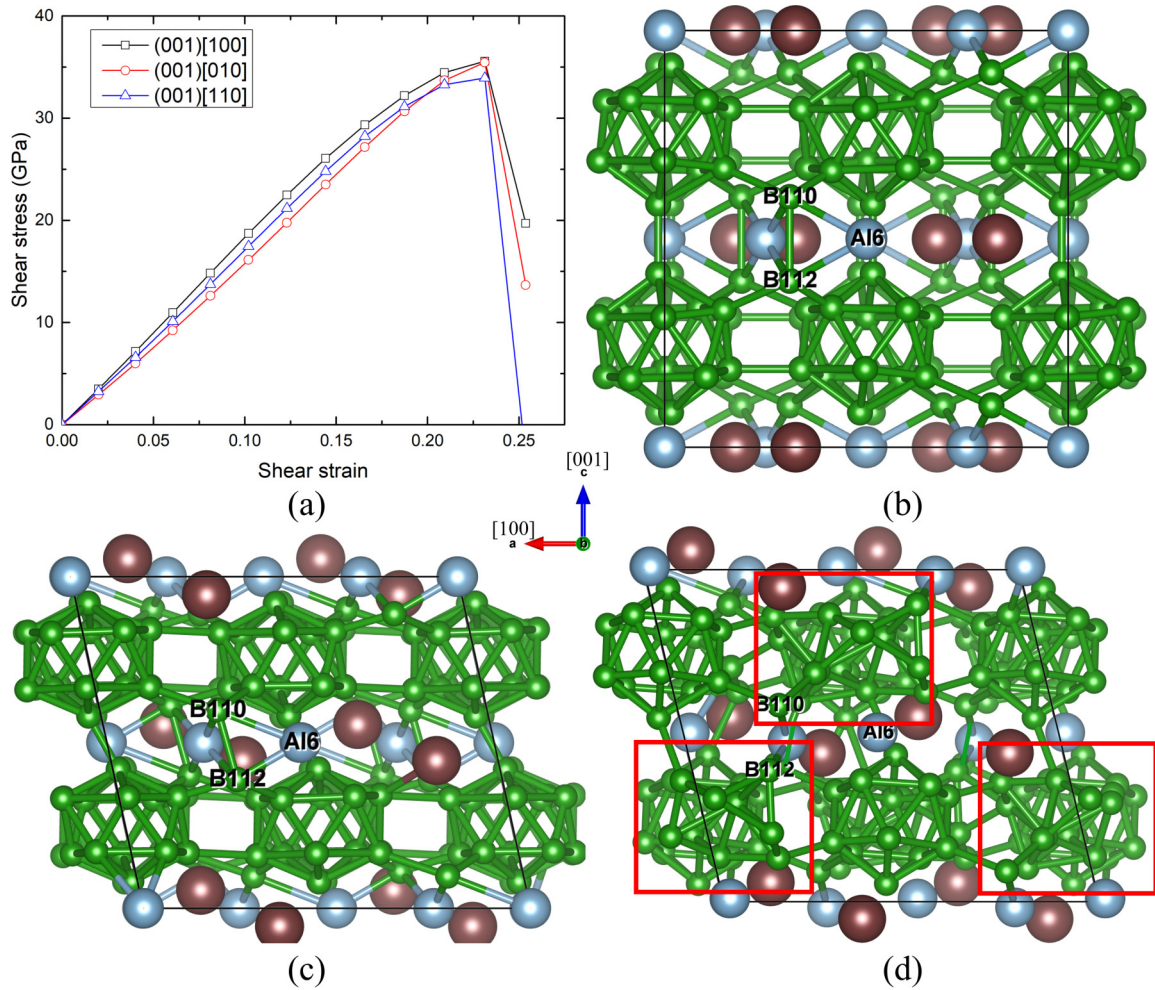


FIG. 5. The shear-stress–shear-strain relationship of AlLiB_{14} under biaxial shear deformation and the structural deformation for shear along the $(001)[110]$ slip system: (a) the shear-stress–shear-strain relationship; (b) the intact structure; (c) the structure at 0.231 shear strain before failure; and (d) the failed structure at 0.254 shear strain in which Al6-B110 and Al6-B112 bonds break while half of the icosahedra are disintegrated.

to the breakage of Al6-B110 and Al6-B112 bonds. The breakage of Al6-B110 and Al6-B112 bonds is also confirmed by bond length change, as shown in Fig. S3(b). The bond stretching ratio of Al6-B110 and Al6-B112 bonds increases from 11.22% and -8.29% to 31.71% and 48.70%, respectively. In addition, half of the icosahedra are deconstructed, suggesting the failure of the system. However, no inter-icosahedral B-B bond breaks at this shear strain, which is consistent with our previous analysis that interlayer B-B bond is stronger than the bonds inside the intra-icosahedral B-B bonds.

We also examined the deformation and failure process of AlLiB_{14} shearing along $(001)[010]$ slip system because the ideal shear strength is only 1.5 GPa higher than that of the $(001)[110]$ slip system. It is also the most plausible failure slip system under pure shear deformation. Figures 6(a)–6(c) display the structural changes under biaxial shear deformation. The intact structure is shown in Fig. 6(a). The B2-B50 bond is stretched from 1.83 to 2.01 Å as shear strain increases to 0.231. But it is not broken, as shown in Fig. 6(b). As the shear strain continuously increases to 0.254, the B2-B50 bond is drastically stretched from 2.01 to 2.83 Å and breaks, as shown in Fig. 6(c). Thus, the deconstruction of the structure along

$(001)[010]$ slip system arises from breaking the B2-B50 bond, which is different from the $(001)[110]$ slip system in which the failure arises from deconstructing icosahedra. However, shear along the $(001)[010]$ slip system is less possible than along the $(001)[110]$ slip system under indentation conditions, since the stress barrier for this slip system is 1.5 GPa higher than the $(001)[110]$ slip system.

E. Deformation and failure of $\text{Al}_{0.75}\text{Mg}_{0.75}\text{B}_{14}$ under biaxial shear deformation

Figure 7(a) displays the shear-stress–shear-strain relationship for $\text{Al}_{0.75}\text{Mg}_{0.75}\text{B}_{14}$ under biaxial shear deformation. The critical shear stresses for $(001)[100]$, $(001)[010]$, and $(001)[110]$ slip systems are 28.7, 26.4, and 28.4 GPa, respectively. Thus, the critical shear stress along the $(001)[010]$ slip system is the lowest among the three selected slip systems, suggesting that it is the most plausible activated slip system for $\text{Al}_{0.75}\text{Mg}_{0.75}\text{B}_{14}$ under indentation conditions. The most plausible slip system changes from $(001)[100]$ under pure shear to $(001)[010]$ under biaxial shear deformation, suggesting that the loading conditions have significant effects

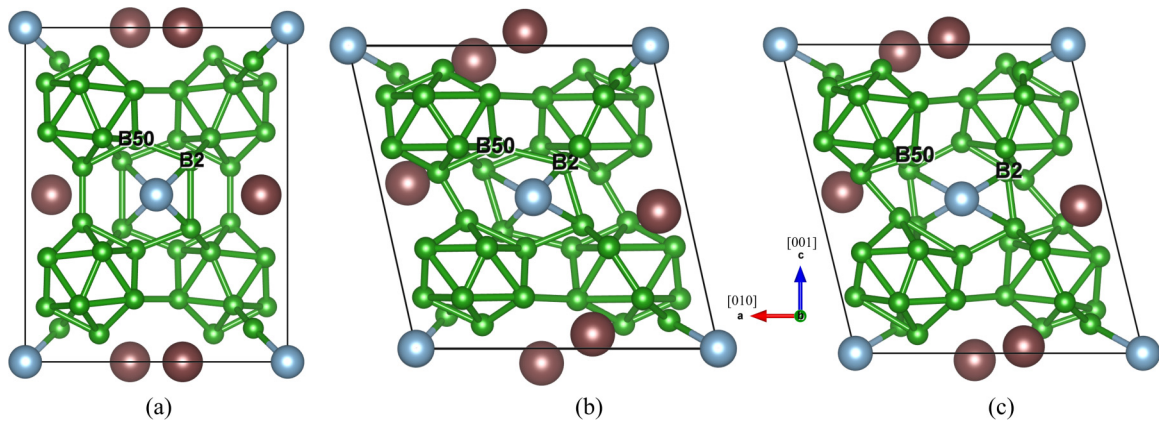


FIG. 6. The structural changes for AlLiB_{14} shearing along the $(001)[010]$ slip system: (a) the intact structure; (b) the structure at 0.231 shear strain corresponding to the maximum of shear stress; and (c) the structure at 0.254 shear strain in which the B2-B50 bond breaks.

on the activated slip system. This is similar to AlLiB_{14} . In addition, the lowest critical shear stress for $\text{Al}_{0.75}\text{Mg}_{0.75}\text{B}_{14}$ is 26.4 GPa, which is lower than that for AlLiB_{14} under biaxial shear deformation. This is consistent with the pure shear deformation, suggesting that metal vacancies lower the strength of orthorhombic borides.

A kink is present in the shear-stress–shear-strain relationship [Fig. 7(a)] for this slip system, suggesting the whole failure process can be divided into two steps. The failure mechanism of $\text{Al}_{0.75}\text{Mg}_{0.75}\text{B}_{14}$ for shear along the $(001)[010]$ slip system under biaxial stress conditions is shown in Figs. 7(b)–7(g).

(1) Figure 7(b) displays the intact structure. With the increase of the shear strain, the system deforms elastically until 0.187 shear strain. Meanwhile, the shear stress reaches

its maximum of 26.4 GPa. No bond is broken as shown in Fig. 7(c). The most stretched bond is the Al3-B16 bond, with the bond length increasing from 2.06 to 2.20 Å. As the shear strain increases to 0.209, the Al3-B16 bond increases to 2.67 Å and breaks. The bond length variation with the increasing shear strain is shown in Fig. S5(b). The bond stretching ratio of Al3-B16 drastically increases from 6.72% to 29.48% at 0.209, suggesting the bond breaking. Meanwhile, the intricosahedral B37-B50 bond increases from 1.79 to 2.00 Å, as shown in Fig. 7(d). As the system is continuously sheared to 0.231 strain, the B37-B50 bond increases to 2.86 Å and breaks, decreasing the shear stress from 25.7 to 20.2 GPa, as shown in Fig. 7(e). This bond breaking is also confirmed by the bond stretching ratio, which drastically increases from 12.12% to 60.33% at 0.231 shear strain, as shown in Fig. S5(b).

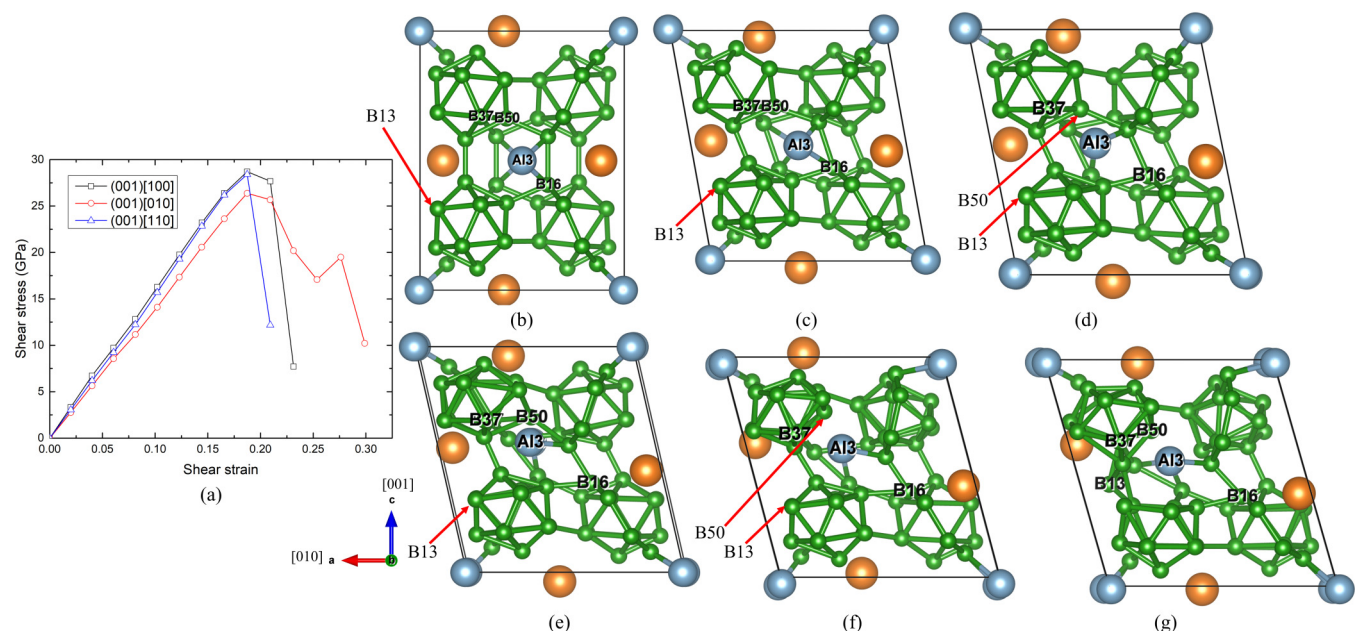


FIG. 7. The shear-stress–shear-strain relationship of $\text{Al}_{0.75}\text{Mg}_{0.75}\text{B}_{14}$ under biaxial shear deformation and the structural deformation for shear along $(001)[010]$ slip system: (a) the shear-stress–shear-strain relationship along three plausible slip systems; (b) the intact structure; (c) the structure at 0.187 shear strain in which the shear stress increases to its maximum and the Al3-B16 bond increases from 2.06 to 2.20 Å; (d) the structure at 0.209 shear strain in which the Al3-B16 bond breaks; (e) the structure at 0.231 shear strain in which the B37-B50 bond breaks; (f) the structure at 0.254 shear strain before failure; (g) the structure at 0.299 shear strain in which the icosahedra are deconstructed.

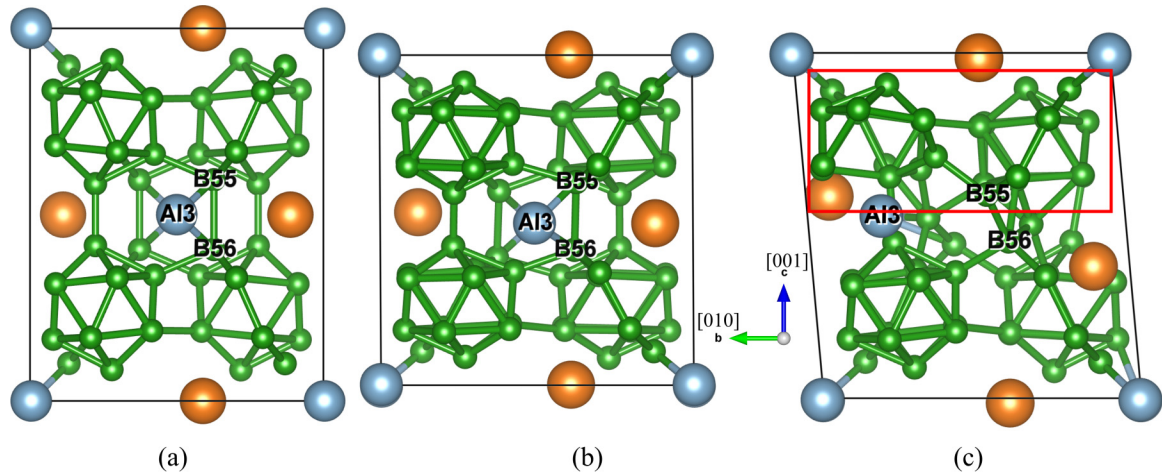


FIG. 8. The structural changes for $\text{Al}_{0.75}\text{Mg}_{0.75}\text{B}_{14}$ shearing along (001)[100] slip system: (a) the intact structure; (b) the structure at 0.209 shear strain corresponding to the maximum of shear stress; (c) the structure at 0.231 shear strain in which half of icosahedra are deconstructed.

However, all the icosahedra are not deconstructed at this shear strain.

(2) As the shear strain continuously increases to 0.254, the structure further deforms without deconstructing icosahedra, as shown in Fig. 7(f). This causes the shear stress to slightly increase from 17.1 to 19.5 GPa. However, as the shear strain further increases to 0.299, one of the icosahedra is disintegrated because the icosahedral B13 atom is stretched out of the icosahedron, leading to structural failure, as shown in Fig. 7(g). This process releases the shear stress from 19.5 to 10.2 GPa.

For the (001)[100] slip system, the stress barrier is 2.3 GPa higher than that for the (001)[100] slip system. However, we still investigated the failure process along this slip system since it is the least shear stress slip system under pure shear deformation. The deformation and failure process are shown

in Figs. 8(a)–8(c). The intact structure is shown in Fig. 8(a). At 0.209 shear strain, the shear stress reaches the maximum value of 28.7 GPa. No bond is broken as shown in Fig. 8(b). At 0.231 shear strain, one layer of B_{12} icosahedra is disintegrated. Meanwhile, the Al3-B55 and Al3-B56 bonds are stretched from 2.06 to 2.87 Å and 3.78 Å and break, leading to structural failure, as shown in Fig. 8(c).

F. Deformation and failure of AlLiB_{14} under tensile deformation

In order to compare the difference of failure mechanism between shear and tensile deformation, we examined the tensile deformation of AlLiB_{14} and $\text{Al}_{0.75}\text{Mg}_{0.75}\text{B}_{14}$. The recent DFT study on $\text{Al}_{0.75}\text{Mg}_{0.75}\text{B}_{14}$ showed that the [001] tensile direction has the lowest ideal strength among the [100], [010], and [001] directions [3,21]. Thus, we examined the tensile

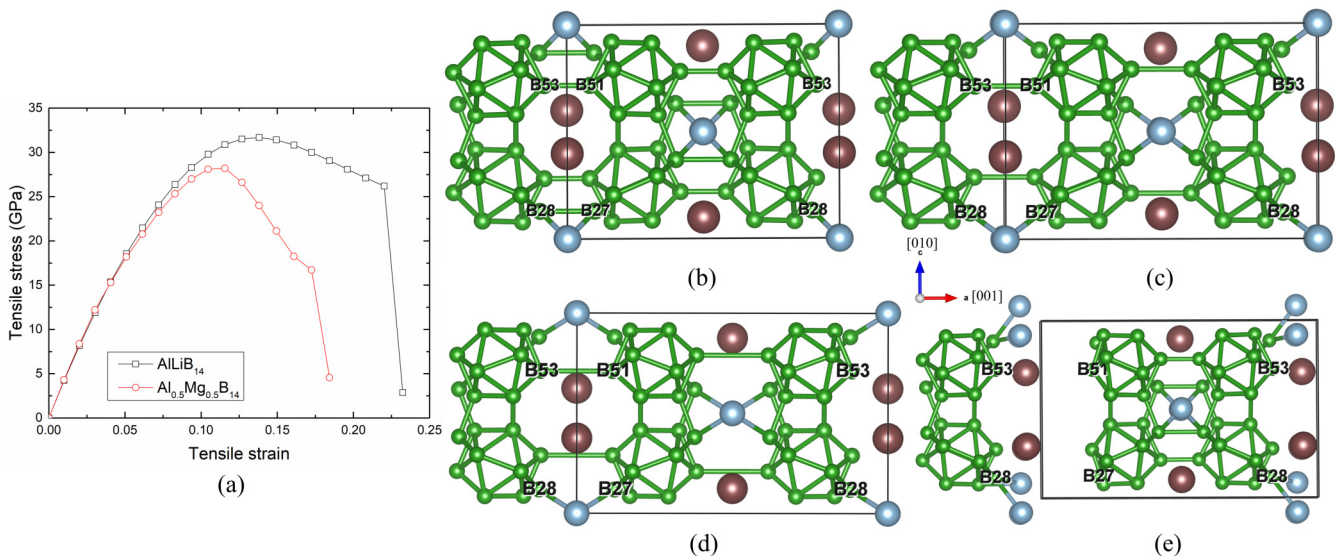


FIG. 9. Tensile-stress–tensile-strain relationship of AlLiB_{14} and $\text{Al}_{0.75}\text{Mg}_{0.75}\text{B}_{14}$ under tensile deformation and the structural changes for AlLiB_{14} : (a) the tensile-stress–tensile-strain relationship for [001] tension; (b) the intact structure of AlLiB_{14} at zero tensile strain; (c) the structure at 0.138 tensile strain in which the shear stress reaches to its maximum and the inter-icosahedra B27-B28 bond breaks; (d) the structure at 0.220 tensile strain in which the B51-B53 bond is stretched from 1.73 to 2.91 Å and all Al-B bonds are stretched from 2.08 to 2.31 Å; (e) the failed structure at 0.232 tensile strain in which all interlayer bonds break.

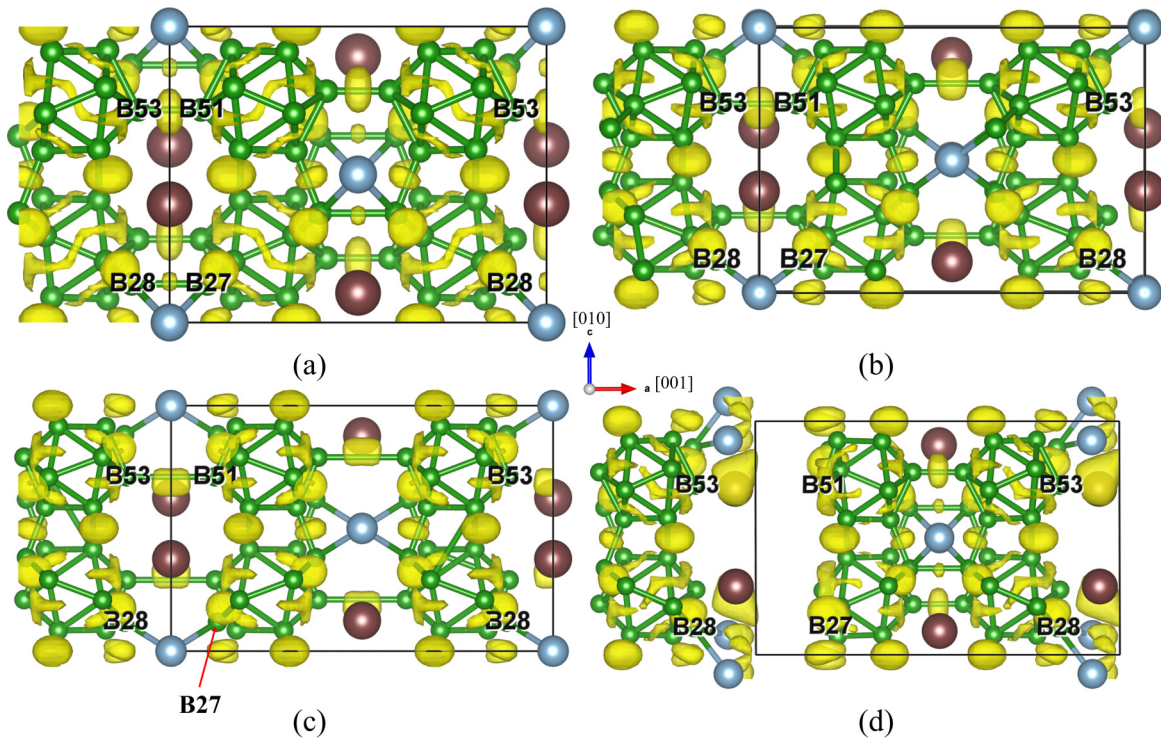


FIG. 10. The isosurface of ELF analysis as a function of tensile strain for AlLiB_{14} : (a) the isosurface of intact structure; (b) the isosurface at 0.138 tensile strain in which no charge concentration between icosahedral B28 and B27 atoms; (c) the isosurface at 0.220 tensile strain; (d) the isosurface at 0.232 tensile strain in which no isosurface can be observed in interlayer region.

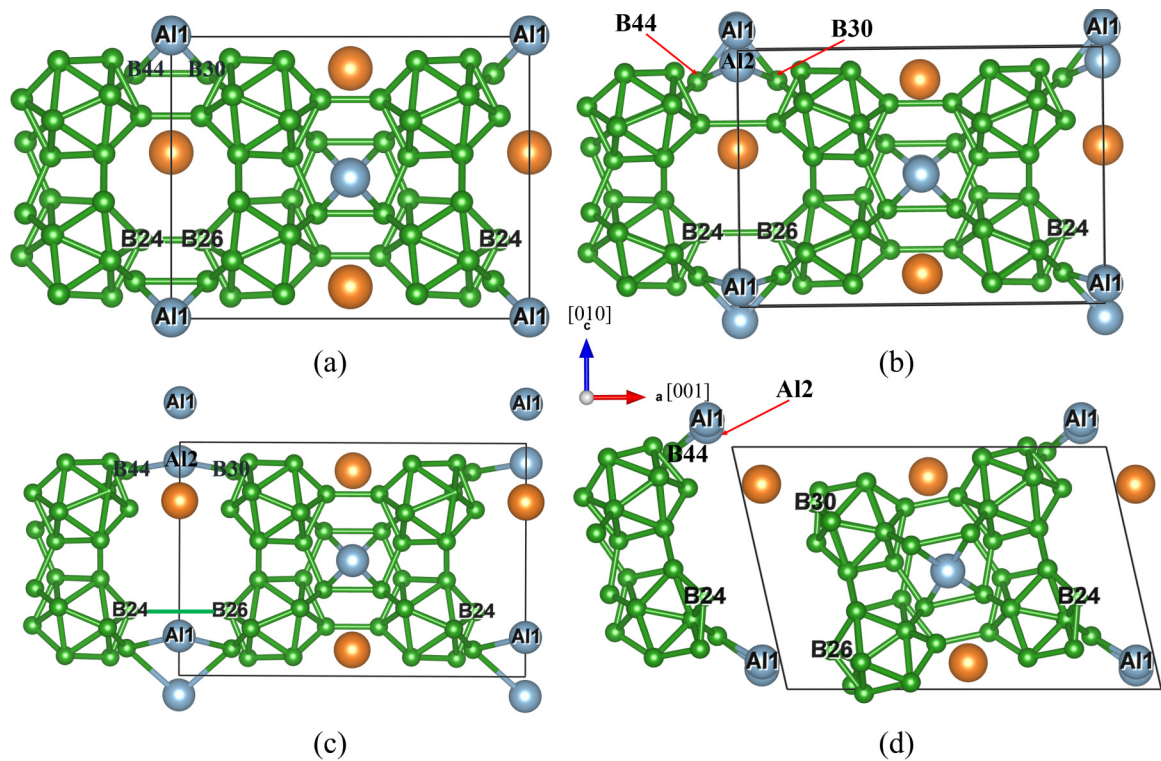


FIG. 11. The structural deformation of $\text{Al}_{0.75}\text{Mg}_{0.75}\text{B}_{14}$ under tensile deformation: (a) the intact structure in which the bond length of inter-icosahedral B30-B44 bond is 2.06 Å; (b) the structure at 0.116 tensile strain in which the tensile stress increases to its maximum and inter-icosahedra B30-B44 bond is stretched to 2.51 Å and breaks; (c) the structure at 0.173 tensile strain in which Al1-B44 and Al1-B30 bonds are broken; (d) the structure at 0.184 tensile strain in which all bonds at interlayer break while Al1-B44 bond forms again.

deformation of AlLiB_{14} and $\text{Al}_{0.75}\text{Mg}_{0.75}\text{B}_{14}$ along the $[00\bar{1}]$ direction. Figure 9(a) displays the stress–strain relationship of AlLiB_{14} and $\text{Al}_{0.75}\text{Mg}_{0.75}\text{B}_{14}$ under $[00\bar{1}]$ tensile deformation. The ideal tensile strength for AlLiB_{14} is 31.7 GPa, which is 3.5 GPa higher than for $\text{Al}_{0.75}\text{Mg}_{0.75}\text{B}_{14}$. This suggests that the $\text{Al}_{0.75}\text{Mg}_{0.75}\text{B}_{14}$ is weaker than AlLiB_{14} .

The fracture process of AlLiB_{14} under $[00\bar{1}]$ tension is shown in Figs. 9(b)–9(e). Figure 9(b) displays the intact structure at zero tensile strain. As tensile strain increases to 0.138, the tensile stress reaches its maximum of 31.7 GPa. The interlayer B27-B28 bond in the B_2 pair is stretched from 2.07 to 2.66 Å and breaks, as shown in Fig. 9(c). At 0.220 tensile strain, the inter-icosahedral B51-B53 bond is stretched from 1.73 Å to 2.91 Å. Meanwhile, all Al-B bonds at interface are also stretched from 2.08 Å to 2.31 Å. But they are not broken, as shown in Fig. 9(d). As the tensile strain continuously increases to 0.232, Al atoms are stretched away from interface along the $[00\bar{1}]$ direction, leading to Al-B bond breakage [Fig. 9(e)]. Meanwhile, the inter-icosahedral B51-B53 bond breaks. The breaking of these bonds leads to the structural failure. The structural failure also releases the tensile stress from 26.2 to 2.9 GPa. To further investigate the bonding change under $[00\bar{1}]$ tension, we applied the ELF analysis on the structures at critical strains. The isosurface of AlLiB_{14} as a function of the tensile strain is shown in Figs. 10(a)–10(d). The isosurface of the intact structure is shown in Fig. 10(a). At 0.138 tensile strain, the isosurface between two interlayer B27 and B28 atoms cannot be observed, suggesting the B27-B28 bond

breaks, as shown in Fig. 10(b). At 0.220 tensile strain, the charge accumulation between the B51-B53 bond that directly connects two icosahedra along the $[00\bar{1}]$ direction is still observed, as shown in Fig. 10(c). At the next tensile strain of 0.232, the isosurface between B51 and B53 atoms disappears [Fig. 10(d)], suggesting the B51-B53 bond is broken. Instead, there is an isosurface close to the Al and Li atoms. The reason is that ionized Al and Li atoms at the interface are stretched away from the B51 atom, leading to part of the bonding electrons transferring back to Al and Li atoms and becoming delocalized near the Li and Al atoms.

G. Deformation and failure of $\text{Al}_{0.75}\text{Mg}_{0.75}\text{B}_{14}$ under tensile deformation

Figures 11(a)–11(d) display the fracture process of $\text{Al}_{0.75}\text{Mg}_{0.75}\text{B}_{14}$ under $[00\bar{1}]$ tension. The intact structure is shown in Fig. 11(a). As the tensile strain increases to 0.116, the tensile stress reaches its maximum value of 28.2 GPa and the inter-icosahedral B30-B44 bond is stretched from 2.06 to 2.51 Å and breaks, as shown in Fig. 11(b). Meanwhile, the Al1-B44 and Al1-B30 bonds increase from 2.11 to 2.33 Å. As the tensile strain continuously increases to 0.173, both Al1-B44 and Al1-B30 bonds break, as shown in Fig. 11(c). At the next tensile strain of 0.184, the inter-icosahedral B24-B26 bond is stretched to 4.77 Å and breaks. Meanwhile, Al1 and Al2 atoms are stretched away from B30 along the $[00\bar{1}]$ direction, which causes the Al2-B30 bond to drastically

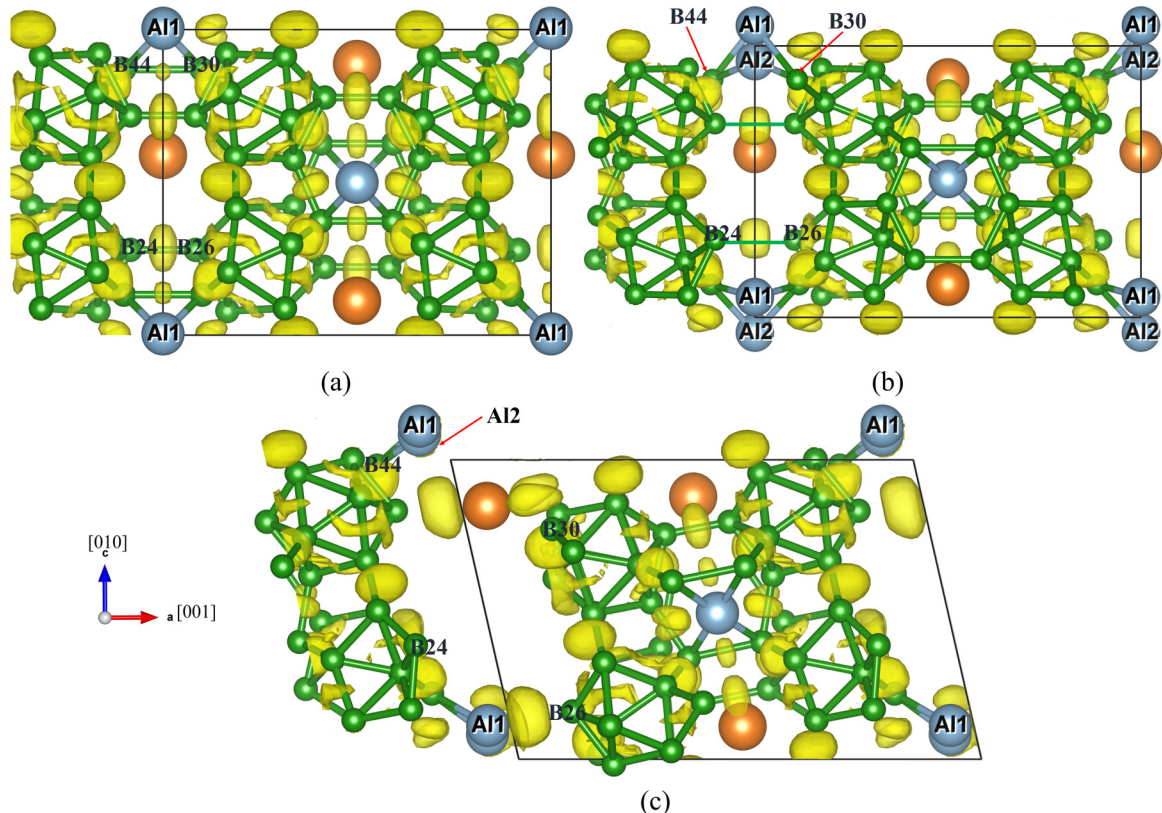


FIG. 12. The isosurface of $\text{Al}_{0.75}\text{Mg}_{0.75}\text{B}_{14}$ as a function of tensile strain: (a) the isosurface of intact structure; (b) the isosurface at 0.116 tensile strain in which no isosurface can be observed between inter-icosahedral B30 and B44 atoms; and (c) the isosurface at 0.184 tensile strain in which the isosurface of Al2-B30 and B24-B26 disappears.

stretch from 2.58 to 5.34 Å and break while the AlI-B44 bond forms again. Thus, the structure is deconstructed, as shown in Fig. 11(d), that releases the tensile stress from 16.7 to 4.6 GPa. It is worth mentioning that the inter-icosahedra B-B bonds do not break during the deformation process, which is different from the failure mechanism of AlLiB₁₄. The isosurface of Al_{0.75}Mg_{0.75}B₁₄ as a function of tensile strain is shown in Figs. 12(a)–12(c). The isosurface of intact structure for Al_{0.75}Mg_{0.75}B₁₄ is shown in Fig. 12(a). At 0.116 tensile strain, the isosurface between the interlayer B30-B44 bond at the interface disappears, suggesting the breaking of the B30-B28 bond, as shown in Fig. 12(b). At 0.184 tensile strain corresponding to the failure of the structure, the isosurface between B24 and B26 atoms cannot be observed, suggesting the breaking of the B24-B26 bond, as shown in Fig. 12(c). However, the isosurface near the Al and Mg atoms can be observed at this shear strain. The reason is that Al and Mg atoms can be ionized and donate valence electrons to inter-icosahedral and interlayer B-B bonds. Thus, the breaking of these bonds delocalized these electrons near the Al and Mg atoms. In addition, the isosurface of inter-icosahedral B-B bonds is observed during the deformation and failure process, which indicates the bonds do not break.

IV. SUMMARY

In summary, we performed PBE-based DFT simulations to examine the failure mechanism of both AlLiB₁₄ and

Al_{0.75}Mg_{0.75}B₁₄ under pure shear, biaxial shear, and tensile deformations. We find that AlLiB₁₄ has a higher critical shear stress than Al_{0.75}Mg_{0.75}B₁₄ under all deformations, suggesting it is stronger than Al_{0.75}Mg_{0.75}B₁₄. In addition, the (001)[010] and (001)[100] are the most plausible slip systems for AlLiB₁₄ and Al_{0.75}Mg_{0.75}B₁₄ under pure shear deformation, respectively. Under biaxial shear conditions, the most plausible slip systems are changed to (001)[110] and (001)[010] for AlLiB₁₄ and Al_{0.75}Mg_{0.75}B₁₄, respectively. The structural failure of both AlLiB₁₄ and Al_{0.75}Mg_{0.75}B₁₄ arises from the icosahedra deconstruction under pure and biaxial shear deformation, while it arises from breaking interlayer bonds between icosahedral layers under tensile deformation. Particularly, the inter-icosahedral B atoms are stretched out of icosahedra for AlLiB₁₄ under pure shear deformation and Al_{0.75}Mg_{0.75}B₁₄ under both pure and biaxial shear deformation, suggesting that the inter-icosahedral B-B bonds are stronger than the intra-icosahedral B-B bonds, which is consistent with the previous Raman spectroscopy and DFT study [12,14].

ACKNOWLEDGMENTS

This work is supported by the Ralph E. Powe Junior Faculty Enhancement Awards from Oak Ridge Associated Universities (ORAU). Q.A. also received support from the U.S. Nuclear Regulatory Commission (NRC-HQ-84-15-G-0028).

-
- [1] S. Vepřek, *J. Vac. Sci. Technol., A* **17**, 2401 (1999).
- [2] B. A. Cook, J. L. Harringa, T. L. Lewis, and A. M. Russell, *Scr. Mater.* **42**, 597 (2000).
- [3] V. I. Ivashchenko, P. E. A. Turchi, S. Veprek, V. I. Shevchenko, J. Leszczynski, L. Gorb, and F. Hill, *J. Appl. Phys.* **119**, 205105 (2016).
- [4] I. Higashi, M. Kobayashi, S. Okada, K. Hamano, and T. Lundström, *J. Cryst. Growth* **128**, 1113 (1993).
- [5] A. M. Russell, B. A. Cook, J. L. Harringa, and T. L. Lewis, *Scr. Mater.* **46**, 629 (2002).
- [6] H. Werheit, V. Filipov, U. Kuhlmann, U. Schwarz, M. Armbrüster, A. Leithe-Jasper, T. Tanaka, I. Higashi, T. Lundström, V. N. Gurin, and M. M. Korsukova, *Sci. Technol. Adv. Mater.* **11**, 023001 (2010).
- [7] L. F. Wan and S. P. Beckman, *Phys. Rev. Lett.* **109**, 145501 (2012).
- [8] J. Emmerlich, N. Thieme, M. to Baben, D. Music, and J. M. Schneider, *J. Phys.: Condens. Matter* **25**, 335501 (2013).
- [9] B. A. Cook, J. S. Peters, J. L. Harringa, and A. M. Russell, *Wear* **271**, 640 (2011).
- [10] Y. Tian, A. F. Bastawros, C. C. H. Lo, A. P. Constant, A. M. Russell, and B. A. Cook, *Appl. Phys. Lett.* **83**, 2781 (2003).
- [11] A. M. Grishin, S. I. Khartsev, J. Böhlmark, and M. Ahlgren, *JETP Lett.* **100**, 680 (2014).
- [12] W. Qu, A. Wu, Z. Wu, Y. Bai, and X. Jiang, *Rare Met.* **31**, 164 (2012).
- [13] H. Kölpin, D. Music, G. Henkelman, and J. M. Schneider, *Phys. Rev. B* **78**, 054122 (2008).
- [14] J. S. Peters, Ph.D. thesis, Iowa State University, 2007.
- [15] X. Jiang, J. Zhao, A. Wu, Y. Bai, and X. Jiang, *J. Phys.: Condens. Matter* **22**, 315503 (2010).
- [16] J. S. Peters, J. M. Hill, and A. M. Russell, *Scr. Mater.* **54**, 813 (2006).
- [17] K. Wade, *J. Chem. Soc. D* **0**, 792 (1971).
- [18] A. J. Welch, *Chem. Commun.* **49**, 3615 (2013).
- [19] Y. Lee and B. N. Harmon, *J. Alloy. Compd.* **338**, 242 (2002).
- [20] L. F. Wan and S. P. Beckman, *Mater. Lett.* **74**, 5 (2012).
- [21] L. F. Wan and S. P. Beckman, *Phys. B: Condens. Matter* **438**, 9 (2014).
- [22] G. Kresse and J. Furthmüller, *Comput. Mater. Sci.* **6**, 15 (1996).
- [23] G. Kresse and J. Furthmüller, *Phys. Rev. B* **54**, 11169 (1996).
- [24] G. Kresse and J. Hafner, *Phys. Rev. B* **47**, 558 (1993).
- [25] J. P. Perdew, K. Burke, and M. Ernzerhof, *Phys. Rev. Lett.* **77**, 3865 (1996).
- [26] G. Kresse and D. Joubert, *Phys. Rev. B* **59**, 1758 (1999).
- [27] P. E. Blöchl, O. Jepsen, and O. K. Andersen, *Phys. Rev. B* **49**, 16223 (1994).
- [28] D. Roundy, C. R. Krenn, M. L. Cohen, and J. W. Morris, Jr., *Phys. Rev. Lett.* **82**, 2713 (1999).
- [29] B. Li, H. Sun, and C. Chen, *Nat. Commun.* **5**, 4965 (2014).
- [30] B. Silvi and A. Savin, *Nature (London)* **371**, 683 (1994).
- [31] K. Momma and F. Izumi, *J. Appl. Crystallogr.* **44**, 1272 (2011).

- [32] See Supplemental Material at <http://link.aps.org/supplemental/10.1103/PhysRevB.98.134105> for the figures of ELF isosurface of AlLiB_{14} , the less stable structure of $\text{Al}_{0.75}\text{Mg}_{0.75}\text{B}_{14}$, the bond changes of AlLiB_{14} and $\text{Al}_{0.75}\text{Mg}_{0.75}\text{B}_{14}$ under shearing, and the stress-strain relationship for both $\text{Al}_{0.75}\text{Li}_{0.75}\text{B}_{14}$ and AlMgB_{14} .
- [33] Q. An and W. A. Goddard, *Phys. Rev. Lett.* **115**, 105501 (2015).
- [34] Q. An and S. I. Morozov, *Phys. Rev. B* **95**, 064108 (2017).
- [35] Q. An, K. M. Reddy, H. Dong, M. W. Chen, A. R. Oganov, and W. A. Goddard, *Nano Lett.* **16**, 4236 (2016).